Nano Research
2023, 16(5): 6353–6360

ISSN 1998-0124 CN 11-5974/O4
https://doi.org/10.1007/s12274-023-5438-z

Research Article

A high-concentrated and nonflammable electrolyte for potassium ion-based dual-graphite batteries

Kexin Li[1,2,§], Guiyou Ma[1,§], Dandan Yu[1] (✉), Wen Luo[1], Jiaxin Li[1], Laishun Qin[1] (✉), Yuexiang Huang[1], and Da Chen[1] (✉)

[1] College of Materials and Chemistry, China Jiliang University, Hangzhou 310018, China
[2] Liangxin College, China Jiliang University, Hangzhou 310018, China
[§] Kexin Li and Guiyou Ma contributed equally to this work.

Received: 25 October 2022 / **Revised:** 5 December 2022 / **Accepted:** 21 December 2022

ABSTRACT

Potassium ion-based dual-graphite batteries (KDGBs) emerge as promising devices for large-scale applications due to their high voltage, low cost, and environmental friendliness. However, conventional KPF_6/carbonate-based electrolytes suffer from severe oxidation decomposition, low concentration, and flammability, which limit the capacity and cyclability of KDGBs. Herein, a nonflammable potassium bis(fluorosulfonyl)imide/triethyl phosphate (KFSI/TEP) electrolyte was designed for KDGBs. When the salt-to-solvent molar ratio increases to 1:1.3, graphite cathode operated at the cut-off potential of 5.2 V exhibits much enhanced capacity, excellent rate capability (26.4 $mAh \cdot g^{-1}$ at 1.0 $A \cdot g^{-1}$), and superior cyclability with 98% capacity retention after 350 cycles. Inorganic compounds-rich electrode/electrolyte interphase layers derived from the preferential decomposition of FSI^- anions ensure good compatibility of the 1:1.3 KFSI/TEP electrolyte with K metal and graphite anodes. Based on this electrolyte, as-assembled KDGBs show high operation voltage of 4.3 V and good cycling performance. This work provides feasibility for developing long-life and safe-operation DGBs.

KEYWORDS

dual-ion batteries, graphite, high voltage, high-concentrated electrolytes, phosphates

1 Introduction

Dual-ion batteries (DIBs), where anions and cations are intercalated/de-intercalated into/from the cathode and anode during the charge/discharge process, respectively, have attracted increasing attention due to their high output voltage and high power [1–3]. In particular, dual-carbon batteries (DCBs) composed of carbonaceous materials as electrodes provide the additional advantages of low cost and environmentally friendliness [4–6]. Owing to the limited lithium (Li) resources (0.0017 wt.%) and their uneven distribution, it is necessary to develop new DCB configurations relying on other alkali metal cations or alkali-earth metal cations. Potassium ion-based DCBs (KDCBs) become a promising candidate for large-scale energy-storage applications because of the similar physicochemical properties between K and Li, comparable redox potentials (−2.93 V for K^+/K and −3.04 V for Li^+/Li), and natural abundant K resources (2.09 wt.%) [7–10].

Benefiting from the high working voltage (> 4.5 V vs. K^+/K) for the anion (de-)intercalation in graphite cathode operated in organic electrolytes, KDCBs are capable of providing a higher output voltage than commercial lithium-ion batteries [8, 11–13]. It should be mentioned that electrolytes play significant roles in influencing the electrochemical performance of KDCBs because both cations and anions originating from electrolytes participate in the electrochemical reaction of two electrodes during the charge/discharge process [14–17]. However, the poor oxidation resistance of conventional carbonate-based electrolytes at high voltages leads to the severe electrolyte decomposition and undesirable cycling performance of KDCBs [18–20]. Moreover, currently carbonate-based electrolytes are volatile and flammable, which bring the potential safety issues. In addition, the large ionic radius of anions (such as PF_6^-, bis(fluorosulfonyl)amide anion (FSI^-), and bis(trifluoromethylsulfonyl)imide anion ($TFSI^-$)) results in the inevitably volume expansion and even exfoliation of graphitic layers after repeated cycling [21]. What is worse, the solvent co-intercalation, especially in low-concentrated electrolytes, usually causes the reduced capacity and cyclability [18, 22]. Besides, the large dissociation energy and strong interaction between K^+ and PF_6^- lead to the low concentration of KPF_6-based electrolytes (≤ 1 $mol \cdot L^{-1}$, 1 M), while the large dosage of these electrolytes limits the energy density of KDCBs [16, 23]. Therefore, developing high-concentrated nonflammable electrolytes with superior anti-oxidation stability is of great significance to improve the capacity, cycling stability, and safety of KDCBs.

Herein, we designed a high-concentrated potassium bis(fluorosulfonyl)imide (KFSI)/triethyl phosphate (TEP) electrolyte for constructing high-safety and low-cost KDCBs based on graphite as both the cathode and anode active materials. The KFSI/TEP electrolyte with the molar ratio of 1:1.3 exhibits a high oxidation potential up to 5.9 V (vs. K^+/K), and enables the significantly enhanced reversible capacity and cycling stability of graphite cathode for FSI^- anion storage. Moreover, inorganic

Address correspondence to Dandan Yu, yudandan@cjlu.edu.cn; Laishun Qin, qinlaishun@cjlu.edu.cn; Da Chen, dchen_80@hotmail.com

compounds-rich electrode/electrolyte interphase layers mainly originating from FSI^- decomposition alleviate the side reactions and improve the reversibility of K platting/stripping as well as the cyclability of K metal anode. When graphite anode is utilized to replace K metal, K^+-based dual-graphite batteries (KDGBs) show high output voltage of 4.3 V and long life for 350 cycles. This work provides a promising DCB candidate with high safety and good cyclability for large-scale energy storage.

2 Experimental section

2.1 Preparation of electrolytes

Different usage amounts of KFSI (Ark) were dissolved in TEP (Alfa) to obtain KFSI/TEP electrolytes with the salt-to-solvent molar ratios of 1:2.0, 1:1.5, and 1:1.3, respectively. All electrolytes were prepared in the Ar-filled glove box with O_2 < 0.01 ppm and H_2O < 0.01 ppm. The conventional 1 M KPF_6/ethylene carbonate-dimethyl carbonate-ethyl methyl carbonate (EC-DMC-EMC, 4:3:2, volume ratio) and 1 M KPF_6/EC-DMC (1:1, volume ratio) electrolytes were purchased from DoDoChem.

2.2 Preparation of graphite electrodes

Graphite cathodes were prepared by mixing the graphite powder (325 mesh, XFNANO), carbon black, and binder at the weight ratio of 80%:10%:10% by using deionized water as dispersing agent to obtain the homogeneous slurry, and then coated on aluminum (Al) foils and dried at 70 °C for 24 h. Three binders including polyvinylidene fluoride (PVDF), sodium alginate (SA), and sodium carboxymethyl cellulose (CMC) were utilized for improving the mechanical stability of graphite cathode through the binder engineering. The mass loading of active material within graphite cathode was around 3.0 mg·cm^{-2}. Graphite anodes coated on Cu foils were fabricated by the same procedure with CMC as binder.

2.3 Electrochemical tests

Stainless steel (SS)//SS cells and K//Al cells with various electrolytes were assembled to evaluate the ionic conductivities and electrochemical stable windows of KFSI/TEP electrolytes with different salt-to-solvent molar ratios, respectively. K//graphite half cells were assembled by using K metal as the anode for evaluating the electrochemical performance of graphite cathode. The KFSI/TEP electrolytes with different salt-to-solvent molar ratios were utilized in K//graphite half cells to improve the anion storage performance of graphite cathode. The performance of graphite anode coated on Cu foils was measured by operating the K//graphite half cells in the voltage range of 0.01–3.0 V (vs. K^+/K). KDGBs with the 1:1.3 KFSI/TEP electrolyte were assembled by coupling graphite cathode with graphite anode at the anode/cathode capacity ratio of 1.1. The current and specific capacities of KDGBs were calculated based on the mass of graphite in cathode. K//Cu cells based on KFSI/TEP electrolytes with different molar ratios were assembled to evaluate the reversibility of K platting/stripping and cycling stability of K metal. The dosage of KFSI/TEP electrolytes for each CR2032 coin cell was 20 μL. Galvanostatic charge/discharge tests were carried out by a Neware CT-4008 battery tester. Cyclic voltammetry (CV), linear sweep voltammetry (LSV), and electrochemical impedance spectroscopy (EIS) measurements were performed on the electrochemical workstation (Autolab 302N).

2.4 Characterization

The solvation structure of KFSI/TEP electrolytes with different molar ratios was characterized by using nuclear magnetic resonance (NMR, AVANCE III HD 600 MHz, dimethyl sulfoxide as the solvent), Raman (inVia-Reflex Raman spectrometer, excitation wavelength: 532 nm), and Fourier transform infrared (FTIR, Nicolet 6700 spectrometer, ATR mode) spectroscopy. X-ray diffraction (XRD) patterns were collected by a SmartLab 9 kW X-ray diffractometer under Cu Kα radiation (λ = 1.5416 Å). To investigate FSI^- intercalation in graphite cathode, K//graphite half cells during the first cycle at 0.1 A·g^{-1} were disassembled in an Ar-filled glove box and then graphite cathodes at different states were obtained for XRD measurement at a scanning speed of 10 °·min^{-1}. X-ray photoelectron spectra (XPS) were collected by using an Escalab 250Xi spectrometer with the Al Kα radiation. Graphite cathodes in half cells after 10 cycles at 0.1 A·g^{-1} to different states were disassembled and subsequently sealed in an air-tight tube after drying to avoid direct contact with air before transporting for XPS characterization. Graphite cathodes after repeated cycling were recycled for XRD and Raman measurements to examine the structural stability of graphite. The morphology and microstructure of samples were observed by using scanning electron microscopy (SEM, Apreo C) and transmission electron microscopy (TEM, Talos F200S).

3 Results and discussion

The ionic conductivities of KFSI/TEP electrolytes with different molar ratios between KFSI and TEP were first evaluated by EIS of SS//SS cells based on various electrolytes (Fig. 1(a)). Although the ionic conductivity of KFSI/TEP electrolytes decreases with the increasing KFSI concentration, it remains as high as 3.98 mS·cm^{-1} when the molar ratio increases to 1:1.3, which is comparable to conventional carbonate-based electrolytes and facilitates the rate capability of the batteries [24, 25]. LSV curves (Fig. 1(b)) of K//Al cells show that the oxidation potential of KFSI/TEP electrolytes can be increased from 4.5 to 5.9 V (vs. K^+/K) as the molar ratio changes from 1:2.0 to 1:1.3, suggesting the enhanced anti-oxidation capability with concentrated KFSI/TEP electrolyte. Nevertheless, when the molar ratio of KFSI/TEP further increases to 1:1.2, the additional KFSI cannot be dissolved in the TEP solvent (Fig. S1 in the Electronic Supplementary Material (ESM)). The flammability tests indicate that the 1 M KPF_6/EC-DMC-EMC electrolyte can be easily ignited. In sharp contrast, the utilization of 1:1.3 KFSI/TEP electrolyte effectively avoids the occurrence of combustion due to the flame resistance of phosphate-based solvents [26, 27], which eliminates safety hazard of the batteries.

The solvation structures of KFSI/TEP electrolytes with various molar ratios were investigated to understand the wide electrochemical stable window at high salt concentrations. As shown in Raman spectra (Fig. S2(a) in the ESM), the typical peak corresponding to the S=O vibration gradually shifts from 1219 to 1223 cm^{-1} as the KFSI/TEP molar ratio increases, resulting from the coordination of K^+ with O in sulfonyl oxygen (S=O) from FSI^- anions [28]. Remarkably, the fraction of free FSI^- decreases with the increasing KFSI concentration (Fig. 1(c)), accompanying with the formation of more contact ion pairs (CIPs) and aggregates (AGGs) in concentrated KFSI/TEP electrolyte [29]. Moreover, FTIR spectra (Fig. 1(d)) show that the intercalation between K^+ and O in P=O bonds leads to the considerable shift of P=O stretching vibration from 1260 to 1250 cm^{-1} after adding KFSI into the TEP solvent [30]. In addition, a downfield trend in ^{19}F chemical shift can be observed with the increasing KFSI/TEP molar ratio (Fig. 1(e)), which is mainly attributed to the weak binding between FSI^- anions and TEP solvent molecules [7, 18, 31]. Simultaneously, the ^{17}O-NMR spectra show that the typical signal of S=O atoms from FSI^- anions slightly shifts from 172.7 to 172.5 ppm with the broad trend as the KFSI/TEP molar ratio

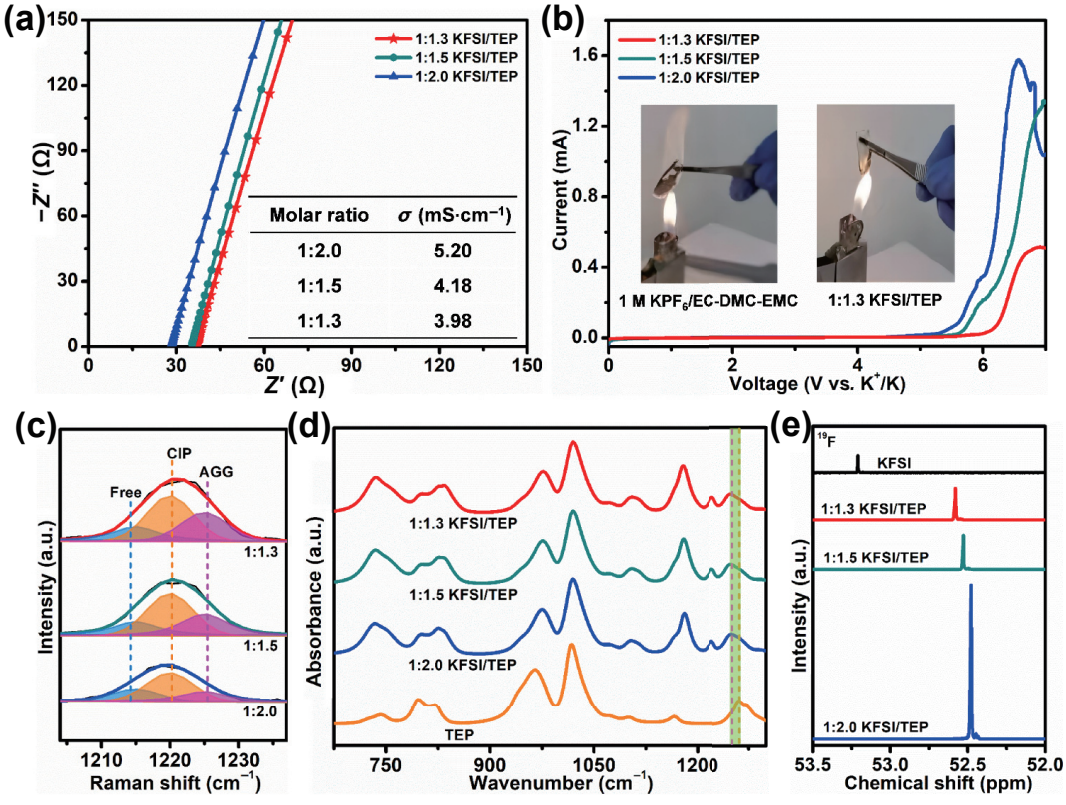

Figure 1 (a) EIS data of SS//SS cells based on KFSI/TEP electrolytes with different salt-to-solvent molar ratios and the corresponding ionic conductivities. (b) LSV curves of K//Al cells based on KFSI/TEP electrolytes with different molar ratios at 1.0 mV·s^{-1} and flammability tests of the 1:1.3 KFSI/TEP electrolyte compared to 1 M KPF_6/EC-DMC-EMC as a typical carbonate-based electrolyte. (c) Raman spectra, (d) FTIR spectra, and (e) ^{19}F NMR spectra of KFSI/TEP electrolytes with different molar ratios compared to pure TEP or KFSI.

increases (Fig. S2(b) in the ESM) due to the enhanced ion–dipole interaction at a high KFSI concentration [32, 33], further indicating the participation of FSI^- anions in the solvation sheath of K^+. All these results demonstrate the strong coordination of K^+–TEP and K^+–FSI^-–TEP complexes in concentrated KFSI/TEP electrolyte.

Because of the large volume change of graphite cathode during repeated anion (de-)intercalation, the mechanical stability of graphite cathode was improved by binder engineering. Three binders including PVDF, SA, and CMC were utilized when preparing graphite cathode. Half cells composed of K metal anode and graphite cathode were assembled to evaluate the FSI^- anion storage performance of graphite cathode. The overall performance of graphite cathodes follows the sequence of CMC > SA > PVDF (Fig. S3 in the ESM), which benefits from the strong interaction of CMC with graphite to improve the mechanical properties of electrodes, and thus graphite cathode with the CMC binder was used for further electrochemical measurements [34]. To confirm the feasibility of KFSI/TEP electrolytes for KDGBs, the electrochemical performance of graphite cathode was evaluated by utilizing KFSI/TEP electrolytes with different molar ratios. Nevertheless, graphite cathode shows poor Coulombic efficiencies (CEs) under the charge cut-off voltage of 5.0 V when using the 1:2.0 KFSI/TEP electrolyte (Figs. S4(a)–S4(c) in the ESM). Notably, the reversible capacity and CEs are effectively promoted as the KFSI/TEP molar ratio increases to 1:1.3 even at 0.5 A·g^{-1} (Figs. S4(d)–S4(f) in the ESM). Moreover, the initial CE increases to 81.9% at 0.5 A·g^{-1}, and the capacity of 40.1 mAh·g^{-1} after 100 cycles can be obtained when the cell was charged to 5.2 V (Fig. 2(a) and Fig. S5(a) in the ESM), where the increase in capacity during the initial cycles might be mainly attributed to the activation process (Fig. S6 in the ESM). However, much decreased CEs happen as the cut-off voltage further increases to 5.3 V (Fig. S7 in the ESM), which is caused by the severe electrolyte oxidative decomposition [35, 36]. Thus, the upper cut-off voltage of graphite cathode in the 1:1.3 KFSI/TEP electrolyte was determined to be 5.2 V for further evaluating the electrochemical performance. Nevertheless, graphite cathode exhibits low capacity and poor CEs when two conventional carbonate-based electrolytes (1 M KPF_6/EC-DMC and 1 M KPF_6/EC-DMC-EMC) are utilized in the same operation window (Fig. S8 in the ESM) because of the electrolyte decomposition at high voltages.

With the utilization of 1:1.3 KFSI/TEP electrolyte, graphite cathode delivers the reversible capacities of 44.4, 40.6, 37.5, 35.5, 29.5, and 26.4 mAh·g^{-1} at 0.2, 0.3, 0.4, 0.5, 0.8, and 1.0 A·g^{-1} (Fig. 2(b) and Fig. S5(b) in the ESM), respectively. The CV curves of graphite cathode remain the same shape at various scan rates (Fig. 2(c)), and meanwhile, the cathodic peak slightly shifts from 4.31 to 4.28 V as the scan rate increases from 0.3 to 1.2 mV·s^{-1}, demonstrating small polarization and fast reaction kinetics of graphite cathode. The current (i) dependence of electrode active materials on the scan rate (v) follows the rule of $i = av^b$ (a and b are variable parameters), where the b value of 0.5 represents that the electrochemical reaction is limited by the diffusion-controlled process, while the b value of 1 indicates the capacitive process. Through the linear fitting, the b values of two dominant oxidation and reduction peaks were determined as 0.797 and 0.893 (Fig. S9 in the ESM), respectively, which suggest that the intercalation of FSI^- anions in graphite cathode has capacitive characteristics. Furthermore, the capacitive contribution can be determined by the equation $i = k_1v + k_2v^{1/2}$, where k_1v and $k_2v^{1/2}$ represent capacitive process and diffusion-controlled process, respectively. In kinetic analysis, the capacitive contribution increases with the scan rate (Fig. 2(d)) and attains 87.8% at 1.2 mV·s^{-1} (Fig. S10 in the ESM), which should be responsible for the high-rate capability of graphite cathode [34]. Importantly, graphite cathode still exhibits the capacity of 32.1 mAh·g^{-1} after 350 cycles at 1.0 A·g^{-1} with a high capacity retention of 98% (Fig. 2(e)) and stable voltage

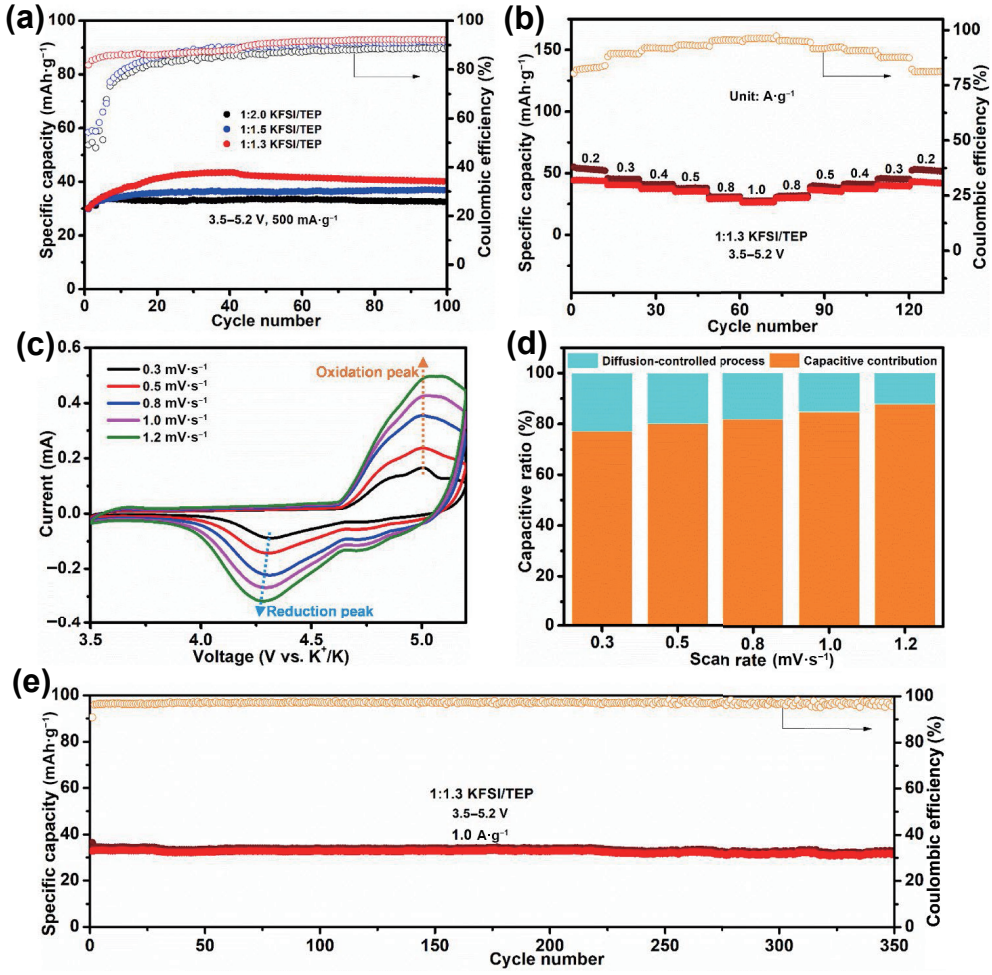

Figure 2 (a) Cycling performance of graphite cathode when utilizing KFSI/TEP electrolytes with different molar ratios at 0.5 A·g^{-1}. (b) Rate capability of graphite cathode when utilizing the 1:1.3 KFSI/TEP electrolyte. (c) CV curves of graphite cathode at different scan rates when using the 1:1.3 KFSI/TEP electrolyte and (d) the corresponding capacitive contribution ratio. (e) Long cycling performance of graphite cathode when utilizing the 1:1.3 KFSI/TEP electrolyte at 1.0 A·g^{-1}.

plateau during cycling (Fig. S11 in the ESM). The overall performance of graphite cathode with the 1:1.3 KFSI/TEP electrolyte is at middle level among the reported literatures (Fig. S12 in the ESM). These results demonstrate that the utilization of concentrated KFSI/TEP electrolyte enables the superior rate performance and cycling stability of graphite cathode.

In order to monitor the structural transformation of graphite cathode during the insertion/extraction process of FSI^- anions, XRD patterns of graphite cathodes at different states were collected during the first cycle at 0.1 A·g^{-1} with the employment of 1:1.3 KFSI/TEP electrolyte. The relative intensity corresponding to the (002) peak of graphite at 26.5° gradually decreases upon charging (Fig. 3(a)). After being charged to the upper voltage limit of 5.2 V (vs. K^+/K), two new peaks emerge at 24.1° and 25.2°, respectively. The interplanar space of graphite cathode increases from 3.35 to 3.69 Å during charging, resulting from the intercalation of FSI^- anions into graphite [37, 38]. The (002) peak of graphite reappears when being discharged to the cut-off voltage of 3.5 V, which suggests the successful de-intercalation of FSI^- anions from graphite. XPS was also performed to detect the compositions of graphite cathodes at the fully charged and discharged states during the 10th cycle. No characteristic peak can be observed from the F 1s spectrum of pristine graphite cathode (Fig. 3(b)) due to the absence of F-containing species. When being charged to 5.2 V, two peaks at 685.2 and 688.3 eV, corresponding to the signals of C–F/S–F/O–F and K–F, appear [16, 39]. The relative content of C–F/S–F/O–F largely decreases after being discharged, which further confirms the FSI^- extraction from graphite cathode [40]. In addition, the main (002) peak of graphite can be well maintained after 10 and 20 cycles (Fig. 3(c)). Moreover, Raman spectra (Fig. 3(d)) show that the E_{2g2} band at 1580 cm^{-1} and 2D band at 2720 cm^{-1} of graphite cathode after cycling recover to the pristine state, which indicates the structural integrity of graphite cathode after the repeated insertion/extraction of FSI^- anions [7, 37].

Furthermore, the morphology of graphite cathode after 350 cycles at 1.0 A·g^{-1} was characterized by TEM (Fig. 3(e)), and a thin cathode/electrolyte interphase (CEI) layer can be detected on the graphite surface (Fig. 3(f)) with the utilization of 1:1.3 KFSI/TEP electrolyte, which helps maintain the structural stability of graphite cathode after long cycling [18, 41]. SEM images (Fig. S13 in the ESM) also prove that the surface of graphite cathode after cycling is completely covered with the CEI film.

Subsequently, the compositions of CEI layer formed on graphite cathode after cycling were investigated by XPS. The S 2p spectra (Fig. 4(a)) can be deconvoluted into characteristic peaks located at 171.2/170.5, 169.4, 167.6, and 163.2 eV, corresponding to the –SON in FSI^- as well as the SO_4^{2-}, SO_3^{2-}, and S^{2-} formed by decomposition of FSI^-, respectively [28, 37, 42]. Moreover, the N 1s spectra (Fig. 4(b)) show two peaks at 400.6 and 399.4 eV assignable to K–N and –SNO groups, respectively [43, 44]. Although the P 2p spectra show the P–O signal originating from TEP decomposition [37, 45], O 1s spectra (Fig. S14 in the ESM) confirm the low content of P-containing species in CEI layer, which suggests the less possibility for solvent decomposition of concentrated KFSI/TEP electrolyte. These results demonstrate that the inorganic compounds rich-CEI layer formed on graphite cathode mainly results from the decomposition of FSI^- anions

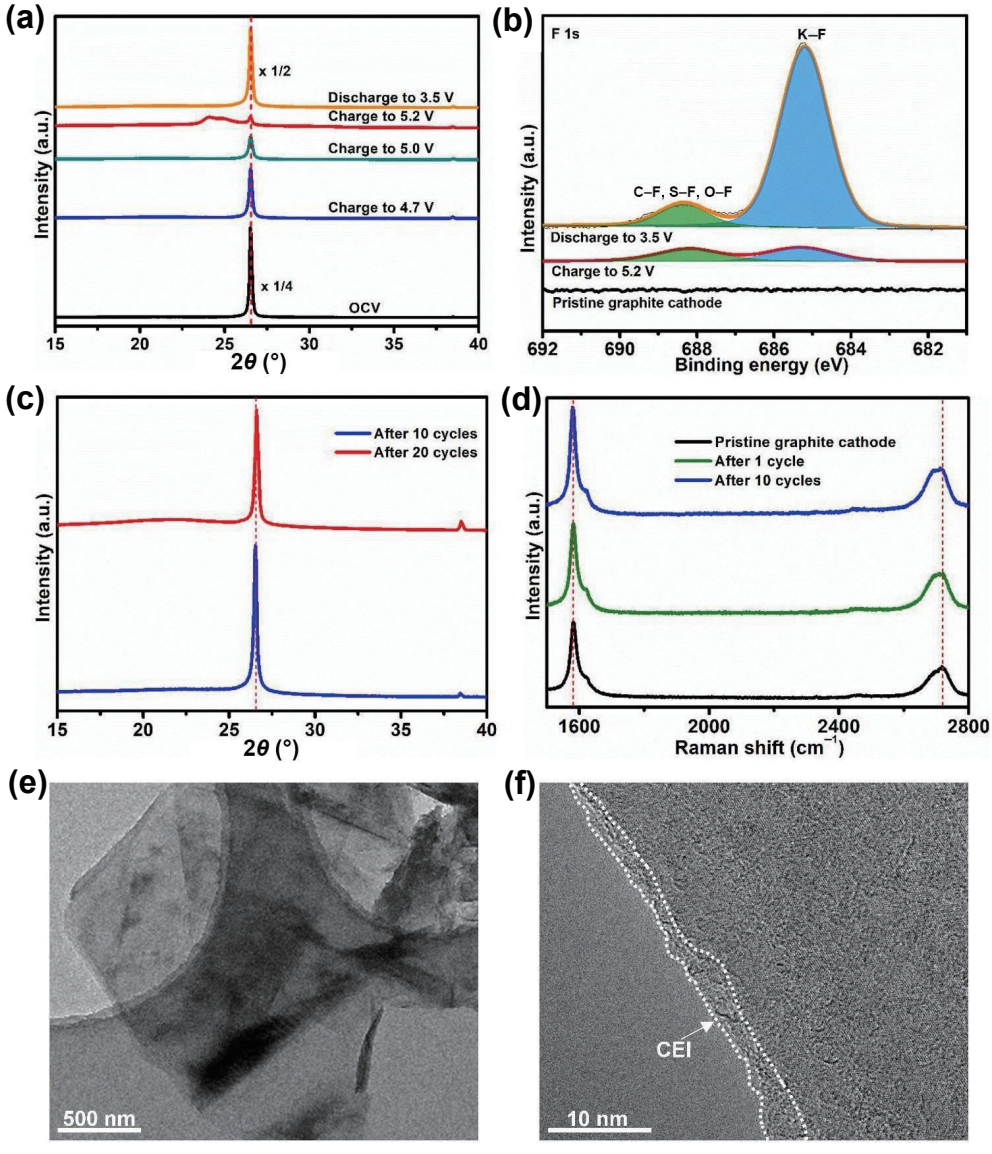

Figure 3 (a) *Ex-situ* XRD patterns of graphite cathodes at different states during the first cycle at 0.1 A·g^{-1} when utilizing the 1:1.3 KFSI/TEP electrolyte. OCV: open circuit voltage. (b) High-resolution F 1s spectra of pristine graphite cathode and the fully charged/discharged graphite cathodes during the 10th cycle at 0.1 A·g^{-1} when utilizing the 1:1.3 KFSI/TEP electrolyte. (c) XRD patterns of graphite cathodes after 10 and 20 cycles at 0.1 A·g^{-1} when utilizing the 1:1.3 KFSI/TEP electrolyte. (d) Raman spectra of pristine graphite cathode and the recycled graphite cathodes after 1 and 10 cycles at 0.1 A·g^{-1} when utilizing the 1:1.3 KFSI/TEP electrolyte. (e) TEM and (f) high-resolution TEM (HRTEM) images of graphite cathode after 350 cycles at 1.0 A·g^{-1} when utilizing the 1:1.3 KFSI/TEP electrolyte.

when the 1:1.3 KFSI/TEP electrolyte is utilized, which possesses good mechanical strength to maintain the structural integrity of graphite cathode during the repeated intercalation/de-intercalation of FSI^- anions [27, 37].

We further investigated the impacts of KFSI/TEP electrolytes with different molar ratios on the cyclability of K metal anode because the above electrochemical performance of graphite cathode was evaluated by assembling half cells based on K metal anode. K//Cu cells with two 1:2.0 and 1:1.5 KFSI/TEP electrolytes show fluctuating CEs after only 286 and 296 cycles at 0.2 mA·cm^{-2} with the platting capacity of 0.2 mAh and the upper potential limit of 1.0 V due to the continuous growth and dissolution of K dendrites (Fig. 4(c)). Remarkably, the utilization of 1:1.3 KFSI/TEP electrolyte enables high CEs of K//Cu cells for 700 cycles, suggesting the enhanced cycling stability of K metal in high-concentrated electrolyte [46, 47]. During the first cycle, the nucleation overpotential (η_n) for the 1:1.3 KFSI/TEP electrolyte is 0.10 V, which is smaller than those of 1:2.0 and 1:1.5 KFSI/TEP electrolytes (Fig. 4(d)), demonstrating that the 1:1.3 KFSI/TEP electrolyte is favorable for K deposition [48, 49]. As the cycling process proceeds, the K platting/stripping profiles of K//Cu cells with the 1:1.3 KFSI/TEP electrolyte exhibit indistinctive change in voltage hysteresis (Fig. 4(e)). Similar phenomenon has been reported in high-concentrated KFSI electrolytes dissolved in carbonate solvents [7], where the formation of FSI^- anion-derived interphase layer contributes to improving the reversibility and cyclability of K metal anode.

Before assembling KDGBs, the compatibility of 1:1.3 KFSI/TEP electrolyte with graphite anode was evaluated in half cells. Graphite anode exhibits superior cycling performance with a high capacity of 281 mAh·g^{-1} after 600 cycles at 0.05 A·g^{-1} (Figs. S15(a) and S15(b) in the ESM). The CV curves of graphite anode at 0.3 mV·s^{-1} show the reversible cathodic/anodic peaks at 0.01 and 0.75 V which are assigned to K^+ insertion and extraction (Fig. S15(c) in the ESM), respectively. By integrating two graphite electrodes with the 1:1.3 KFSI/TEP electrolyte, the working voltage of KDGB is estimated to be around 4.3 V according to the CV curves (Fig. 5(a)) and charge–discharge profiles (Fig. 5(b)) of two half cells. In the KDGB system, FSI^- anions are intercalated into graphite cathode upon charging, while K^+ cations are inserted into graphite anode simultaneously (Fig. 5(c)). During discharge, FSI^- anions and K^+ cations are de-intercalated from two graphite

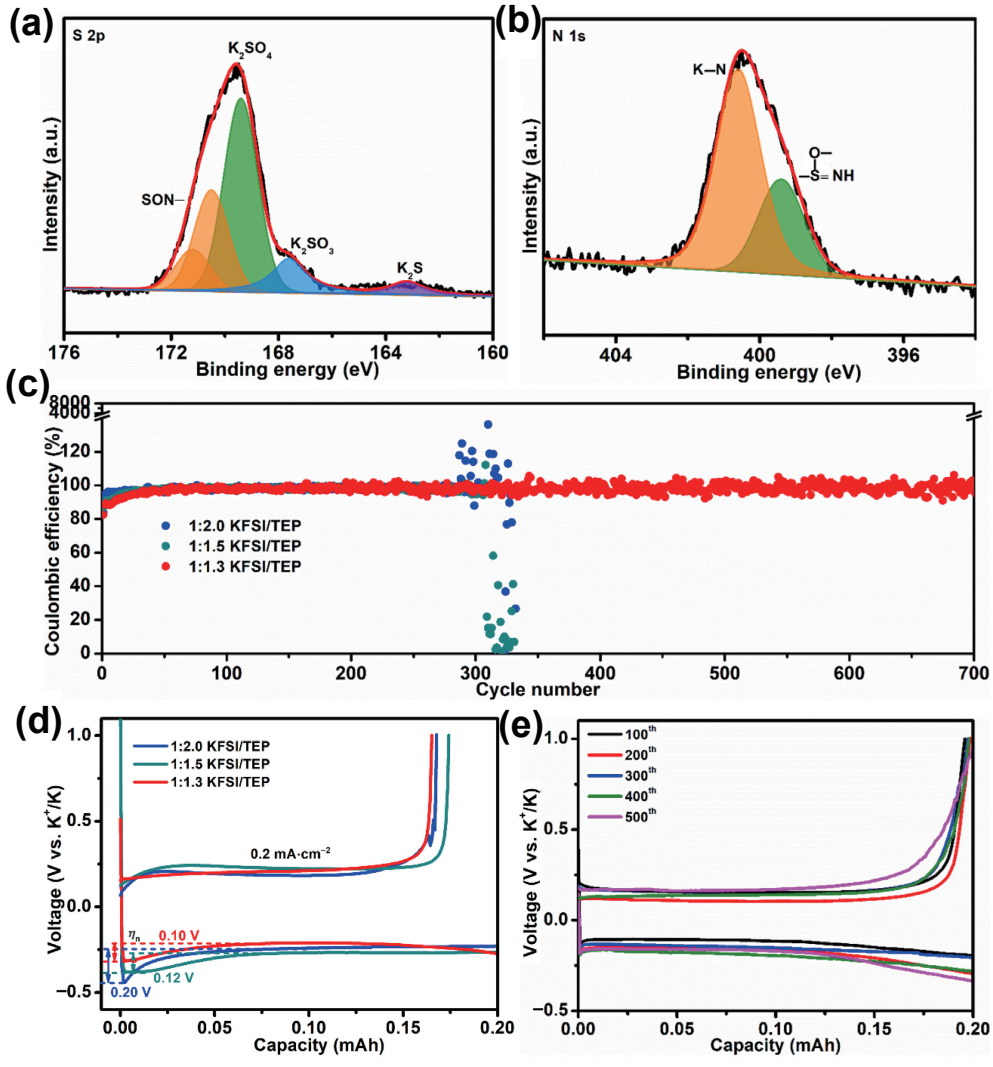

Figure 4 High-resolution (a) S 2p and (b) N 1s spectra of the fully discharged graphite cathode after 10 cycles at 0.1 A·g^{-1} when utilizing the 1:1.3 KFSI/TEP electrolyte. (c) CEs, (d) plating/stripping profiles for initial CEs of K//Cu cells when utilizing KFSI/TEP electrolytes with different molar ratios at 0.2 mA·cm^{-1} with the plating capacity of 0.2 mAh and the charge cut-off voltage of 1.0 V, as well as (e) the representative plating/stripping profiles of K//Cu cells based on the 1:1.3 KFSI/TEP electrolyte.

electrodes back to the electrolyte. Both the current and specific capacities of KDGBs are calculated based on the mass of graphite active material in cathode. The charge/discharge profiles of KDGBs show the high average operating voltage of 4.3 V when operated at 0.5 A·g^{-1} (Fig. 5(d)). The KDGBs deliver the reversible capacity of 26.6 mAh·g^{-1} after 350 cycles at 0.5 A·g^{-1} (Fig. 5(e)). An increase in CEs during the initial cycles can be found, which is primarily due to the electrolyte decomposition for constructing electrode/electrolyte interphase layers. This phenomenon was also found in previous reported DIB systems [20, 38, 50–52]. The good electrochemical performance of as-assembled KDGBs can be mainly attributed to the excellent anti-oxidation capability of the 1:1.3 KFSI/TEP electrolyte and the formation of FSI^--derived interphase layers to suppress further electrolyte decomposition.

4 Conclusions

In summary, a nonflammable phosphate-based electrolyte was successfully designed for K^+-based dual-graphite batteries. With the assistance of CMC binder, the 1:1.3 KFSI/TEP electrolyte endows graphite cathode with high capacity as well as superior rate capability and cyclability under the high cut-off voltage of 5.2 V. *Ex-situ* XRD and XPS prove the reversible FSI^- anion intercalation into graphite cathode. SEM, TEM, and XPS analyses suggest that the FSI^--derived inorganic compound-rich interphase layer formed on the surface of graphite cathode effectively prevents the electrolyte oxidative decomposition at high voltages and maintains the structural stability of graphite cathode during repeated cycling. Moreover, the 1:1.3 KFSI/TEP electrolyte also exhibits good compatibility with both the K metal and graphite anodes. The KDGBs with the 1:1.3 KFSI/TEP electrolyte show a high working voltage around 4.3 V, the reversible capacity up to 45.5 mAh·g^{-1} (based on the graphite in cathode), and good cycling performance for 350 cycles at 0.1 A·g^{-1}. This work demonstrates the feasibility of using nonflammable concentrated electrolytes to develop high-voltage, low-cost, and environmentally friendly DIB systems with high safety for large-scale energy storage applications.

Acknowledgements

The authors acknowledge the financial support of the National Natural Science Foundation of China (Nos. 52002081, 51972294, and 51872271).

Electronic Supplementary Material: Supplementary material (digital photos, Raman spectra and NMR of electrolytes, electrochemical data, and SEM images) is available in the online version of this article at https://doi.org/10.1007/s12274-023-5438-z.

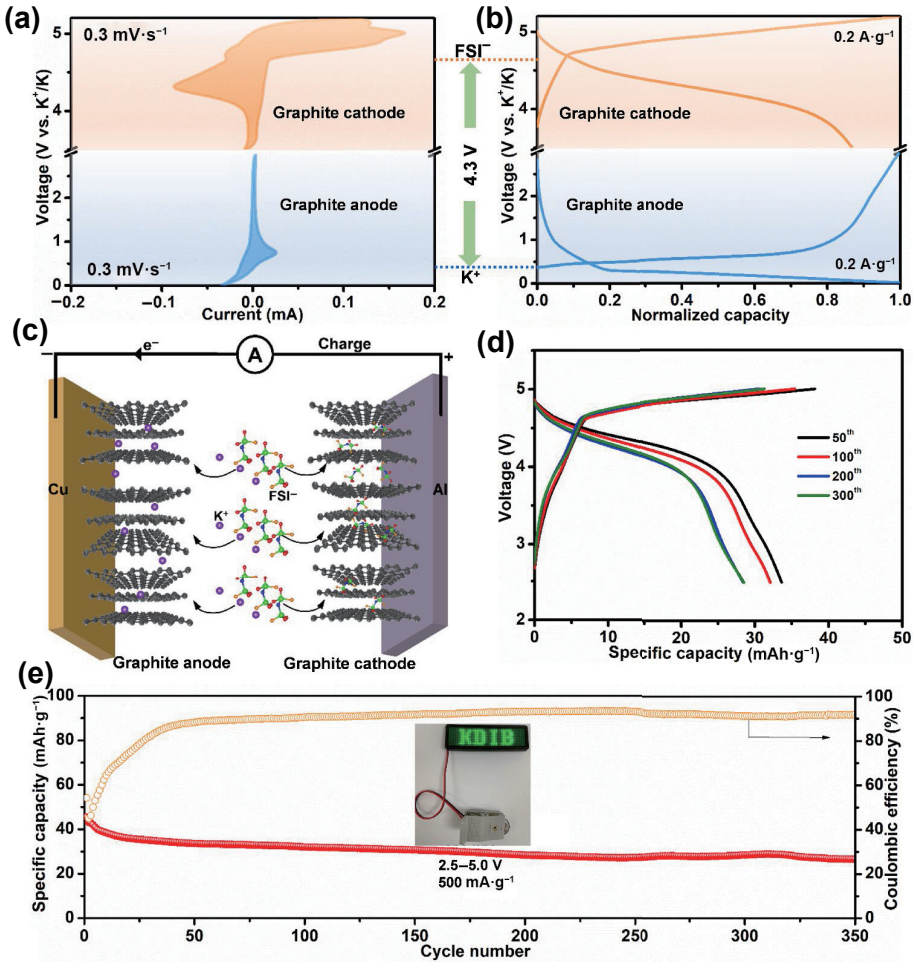

Figure 5 (a) CV curves of graphite anode and graphene cathode in half cells at 0.3 mV·s^{-1} when utilizing the 1:1.3 KFSI/TEP electrolyte. (b) Charge/discharge profiles of graphite anode and graphite cathode in half cells after cycling at 0.2 A·g^{-1} when using the 1:1.3 KFSI/TEP electrolyte. (c) Schematic illustration for the working mechanism of KDGBs. (d) The representative charge/discharge profiles of KDGBs during cycling at 0.5 A·g^{-1} when utilizing the 1:1.3 KFSI/TEP electrolyte, and (e) their cycling performance (inset: the demonstration of LED light powered by one KDGB).

References

[1] Yang, K.; Jia, L. L.; Liu, X. H.; Wang, Z. J.; Wang, Y.; Li, Y. W.; Chen, H. B.; Wu, B.; Yang, L. Y.; Pan, F. Revealing the anion intercalation behavior and surface evolution of graphite in dual-ion batteries via *in situ* AFM. *Nano Res.* **2020**, *13*, 412–418.

[2] Liu, Y. J.; Hu, X.; Li, J. W.; Zhong, G. B.; Yuan, J.; Zhan, H. B.; Tang, Y. B.; Wen, Z. H. Carbon-coated $MoS_{1.5}Te_{0.5}$ nanocables for efficient sodium-ion storage in non-aqueous dual-ion batteries. *Nat. Commun.* **2022**, *13*, 663.

[3] Li, W. H.; Li, Y. M.; Liu, X. F.; Gu, Z. Y.; Liang, H. J.; Zhao, X. X.; Guo, J. Z.; Wu, X. L. All-climate and ultrastable dual-ion batteries with long life achieved via synergistic enhancement of cathode and anode interfaces. *Adv. Funct. Mater.* **2022**, *32*, 2201038.

[4] Chen, S. H.; Kuang, Q.; Fan, H. J. Dual-carbon batteries: Materials and mechanism. *Small* **2020**, *16*, 2002803.

[5] Ji, B. F.; Zhang, F.; Wu, N. Z.; Tang, Y. B. A dual-carbon battery based on potassium-ion electrolyte. *Adv. Energy Mater.* **2017**, *7*, 1700920.

[6] Hou, R. L.; Liu, B.; Sun, Y. L.; Liu, L. Y.; Meng, J. N.; Levi, M. D.; Ji, H. X.; Yan, X. B. Recent advances in dual-carbon based electrochemical energy storage devices. *Nano Energy* **2020**, *72*, 104728.

[7] Yu, D. D.; Zhang, W.; Zhang, Q.; Huang, S. M. Tuning anion chemistry enables high-voltage and stable potassium-based tellurium-graphite batteries. *Nano Energy* **2022**, *92*, 106744.

[8] Zhu, J. J.; Li, Y. L.; Yang, B. J.; Liu, L. Y.; Li, J. S.; Yan, X. B.; He, D. Y. A dual carbon-based potassium dual ion battery with robust comprehensive performance. *Small* **2018**, *14*, 1801836.

[9] Liu, M. Q.; Chang, L. M.; Le, Z. Y.; Jiang, J. M.; Li, J. H.; Wang, H. R.; Zhao, C. M.; Xu, T. H.; Nie, P.; Wang, L. M. Emerging potassium-ion hybrid capacitors. *ChemSusChem* **2020**, *13*, 5837–5862.

[10] Ruan, J. F.; Mo, F. J.; Chen, Z. L.; Liu, M.; Zheng, S. Y.; Wu, R. B.; Fang, F.; Song, Y.; Sun, D. L. Rational construction of nitrogen-doped hierarchical dual-carbon for advanced potassium-ion hybrid capacitors. *Adv. Energy Mater.* **2020**, *10*, 1904045.

[11] Yang, K.; Liu, Q. R.; Zheng, Y. P.; Yin, H.; Zhang, S. Q.; Tang, Y. B. Locally ordered graphitized carbon cathodes for high-capacity dual-ion batteries. *Angew. Chem., Int. Ed.* **2021**, *60*, 6326–6332.

[12] Fan, L.; Liu, Q.; Chen, S. H.; Lin, K. R.; Xu, Z.; Lu, B. A. Potassium-based dual ion battery with dual-graphite electrode. *Small* **2017**, *13*, 1701011.

[13] Zhu, J. J.; Xu, Y. T.; Fu, Y. J.; Xiao, D. W.; Li, Y. L.; Liu, L. Y.; Wang, Y.; Zhang, Q. N.; Li, J. S.; Yan, X. B. Hybrid aqueous/nonaqueous water-in-bisalt electrolyte enables safe dual ion batteries. *Small* **2020**, *16*, 1905838.

[14] Obrezkov, F. A.; Shestakov, A. F.; Vasil'ev, S. G.; Stevenson, K. J.; Troshin, P. A. Polydiphenylamine as a promising high-energy cathode material for dual-ion batteries. *J. Mater. Chem. A* **2021**, *9*, 2864–2871.

[15] Zhang, L.; Wang, H. Y. Intercalation of multiply solvated hexafluorophospate anion into graphite electrode from mixtures of methyl acetate, ethyl methyl, and ethylene carbonates. *J. Energy Chem.* **2021**, *58*, 233–236.

[16] Li, X.; Ou, X. W.; Tang, Y. B. 6.0 V high-voltage and concentrated electrolyte toward high energy density K-based dual-graphite battery. *Adv. Energy Mater.* **2020**, *10*, 2002567.

[17] Huang, Z. D.; Hou, Y.; Wang, T. R.; Zhao, Y. W.; Liang, G. J.; Li, X. L.; Guo, Y.; Yang, Q.; Chen, Z.; Li, Q. et al. Manipulating anion intercalation enables a high-voltage aqueous dual ion battery. *Nat. Commun.* **2021**, *12*, 3106.

[18] Yu, D. D.; Zhu, Q. N.; Cheng, L. W.; Dong, S.; Zhang, X. H.; Wang,

H.; Yang, N. J. Anion solvation regulation enables long cycle stability of graphite cathodes. *ACS Energy Lett.* **2021**, *6*, 949–958.
[19] Cheng, Z. J.; Guo, L. F.; Dong, Q. Y.; Wang, C. T.; Yao, Q.; Gu, X.; Yang, J.; Qian, Y. T. Highly durable and ultrafast cycling of dual-ion batteries via *in situ* construction of cathode–electrolyte interphase. *Adv. Energy Mater.* **2022**, *12*, 2202253.
[20] Wang, Y.; Zhang, Y. J.; Wang, S.; Dong, S. Y.; Dang, C. Q.; Hu, W. C.; Yu, D. Y. W. Ultrafast charging and stable cycling dual-ion batteries enabled via an artificial cathode–electrolyte interface. *Adv. Funct. Mater.* **2021**, *31*, 2102360.
[21] Kravchyk, K. V.; Bhauriyal, P.; Piveteau, L.; Guntlin, C. P.; Pathak, B.; Kovalenko, M. V. High-energy-density dual-ion battery for stationary storage of electricity using concentrated potassium fluorosulfonylimide. *Nat. Commun.* **2018**, *9*, 4469.
[22] Han, X. Q.; Xu, G. J.; Zhang, Z. H.; Du, X. F.; Han, P. X.; Zhou, X. H.; Cui, G. L.; Chen, L. Q. An *in situ* interface reinforcement strategy achieving long cycle performance of dual-ion batteries. *Adv. Energy Mater.* **2019**, *9*, 1804022.
[23] Tan, H.; Zhai, D. Y.; Kang, F. Y.; Zhang, B. Synergistic PF_6^- and FSI^- intercalation enables stable graphite cathode for potassium-based dual ion battery. *Carbon* **2021**, *178*, 363–370.
[24] Zheng, X. Y.; Gu, Z. Y.; Fu, J.; Wang, H. T.; Ye, X. L.; Huang, L. Q.; Liu, X. Y.; Wu, X. L.; Luo, W.; Huang, Y. H. Knocking down the kinetic barriers towards fast-charging and low-temperature sodium metal batteries. *Energy Environ. Sci.* **2021**, *14*, 4936–4947.
[25] Holoubek, J.; Yin, Y. J.; Li, M. Q.; Yu, M. Y.; Meng, Y. S.; Liu, P.; Chen, Z. Exploiting mechanistic solvation kinetics for dual-graphite batteries with high power output at extremely low temperature. *Angew. Chem., Int. Ed.* **2019**, *58*, 18892–18897.
[26] Naveed, A.; Yang, H. J.; Yang, J.; Nuli, Y. N.; Wang, J. L. Highly reversible and rechargeable safe Zn batteries based on a triethyl phosphate electrolyte. *Angew. Chem., Int. Ed.* **2019**, *58*, 2760–2764.
[27] Ou, X. W.; Li, J.; Tong, X. Y.; Zhang, G.; Tang, Y. B. Highly concentrated and nonflammable electrolyte for high energy density K-based dual-ion battery. *ACS Appl. Energy Mater.* **2020**, *3*, 10202–10208.
[28] Liu, S. L.; Mao, J. F.; Zhang, Q.; Wang, Z. J.; Pang, W. K.; Zhang, L.; Du, A. J.; Sencadas, V.; Zhang, W. C.; Guo, Z. P. An intrinsically non-flammable electrolyte for high-performance potassium batteries. *Angew. Chem., Int. Ed.* **2020**, *59*, 3638–3644.
[29] Zeng, Z. Q.; Murugesan, V.; Han, K. S.; Jiang, X. Y.; Cao, Y. L.; Xiao, L. F.; Ai, X. P.; Yang, H. X.; Zhang, J. G.; Sushko, M. L. et al. Non-flammable electrolytes with high salt-to-solvent ratios for Li-ion and Li-metal batteries. *Nat. Energy* **2018**, *3*, 674–681.
[30] Seggem, P.; Jetti, V. R.; Basak, P. Nonflammable and stable quasi-solid electrolytes: Demonstrating the feasibility of application in rechargeable solid-state magnesium batteries. *ACS Appl. Energy Mater.* **2022**, *5*, 6606–6617.
[31] Jia, M. M.; Zhang, C.; Guo, Y. W.; Peng, L. S.; Zhang, X. Y.; Qian, W. W.; Zhang, L.; Zhang, S. J. Advanced nonflammable localized high-concentration electrolyte for high energy density lithium battery. *Energy Environ. Mater.* **2022**, *5*, 1294–1302.
[32] Tsubouchi, S.; Suzuki, S.; Nishimura, K.; Okumura, T.; Abe, T. Effect of Lewis acids on graphite-electrode properties in EC-based electrolyte solutions with organophosphorus compounds. *J. Electrochem. Soc.* **2018**, *165*, A680–A687.
[33] Yu, D. D.; Wang, H.; Zhang, W.; Dong, H. F.; Zhu, Q. N.; Yang, J.; Huang, S. Unraveling the role of ion-solvent chemistry in stabilizing small-molecule organic cathode for potassium-ion batteries. *Energy Storage Mater.* **2021**, *43*, 172–181.
[34] Wang, G.; Yu, M. H.; Wang, J. G.; Li, D. B.; Tan, D. M.; Löffler, M.; Zhuang, X. D.; Mullen, K.; Feng, X. L. Self-activating, capacitive anion intercalation enables high-power graphite cathodes. *Adv. Mater.* **2018**, *30*, 1800533.
[35] Read, J. A.; Cresce, A. V.; Ervin, M. H.; Xu, K. Dual-graphite chemistry enabled by a high voltage electrolyte. *Energy Environ. Sci.* **2014**, *7*, 617–620.
[36] Qiao, Y.; Jiang, K. Z.; Li, X.; Deng, H.; He, Y. B.; Chang, Z.; Wu, S. C.; Guo, S. H.; Zhou, H. S. A hybrid electrolytes design for capacity-equivalent dual-graphite battery with superior long-term cycle life. *Adv. Energy Mater.* **2018**, *8*, 1801120.
[37] Jiang, X. Y.; Liu, X. W.; Zeng, Z. Q.; Xiao, L. F.; Ai, X. P.; Yang, H. X.; Cao, Y. L. A nonflammable Na^+-based dual-carbon battery with low-cost, high voltage, and long cycle life. *Adv. Energy Mater.* **2018**, *8*, 1802176.
[38] Wrogemann, J. M.; Haneke, L.; Ramireddy, T.; Frerichs, J. E.; Sultana, I.; Chen, Y. I.; Brink, F.; Hansen, M. R.; Winter, M.; Glushenkov, A. M. et al. Advanced dual-ion batteries with high-capacity negative electrodes incorporating black phosphorus. *Adv. Sci.* **2022**, *9*, 2201116.
[39] Wang, H.; Yu, D. D.; Wang, X.; Niu, Z. Q.; Chen, M. X.; Cheng, L. W.; Zhou, W.; Guo, L. Electrolyte chemistry enables simultaneous stabilization of potassium metal and alloying anode for potassium-ion batteries. *Angew. Chem., Int. Ed.* **2019**, *58*, 16451–16455.
[40] Wang, W.; Huang, H. X.; Wang, B.; Qian, C.; Li, P. H.; Zhou, J. H.; Liang, Z. B.; Yang, C.; Guo, S. J. A new dual-ion battery based on amorphous carbon. *Sci. Bull.* **2019**, *64*, 1634–1642.
[41] Liu, T. M.; Han, X. Q.; Zhang, Z. H.; Chen, Z.; Wang, P.; Han, P. X.; Ding, N. X.; Cui, G. L. A high concentration electrolyte enables superior cycleability and rate capability for high voltage dual graphite battery. *J. Power Sources* **2019**, *437*, 226942.
[42] Ji, S. P.; Li, J. L.; Li, J. F.; Song, C. Y.; Wang, S.; Wang, K. X.; Hui, K. S.; Zha, C. Y.; Zheng, Y. S.; Dinh, D. A. et al. Dynamic reversible evolution of solid electrolyte interface in nonflammable triethyl phosphate electrolyte enabling safe and stable potassium-ion batteries. *Adv. Funct. Mater.* **2022**, *32*, 2200771.
[43] Wang, Z. J.; Wang, Y. Y.; Li, B. H.; Bouwer, J. C.; Davey, K.; Lu, J.; Guo, Z. P. Non-flammable ester electrolyte with boosted stability against Li for high-performance Li metal batteries. *Angew. Chem., Int. Ed.* **2022**, *61*, e202206682.
[44] Zhang, X. Y.; Jia, M. M.; Zhang, Q. P.; Zhang, N. N.; Wu, X. K.; Qi, S. T.; Zhang, L. $LiNO_3$ and TMP enabled high voltage room-temperature solid-state lithium metal battery. *Chem. Eng. J.* **2022**, *448*, 137743.
[45] Asfaw, H. D.; Kotronia, A. A polymeric cathode–electrolyte interface enhances the performance of MoS_2-graphite potassium dual-ion intercalation battery. *Cell Rep. Phys. Sci.* **2022**, *3*, 100693.
[46] Zhao, Y.; Liu, B. Z.; Yi, Y. Y.; Lian, X. Y.; Wang, M. L.; Li, S.; Yang, X. Z.; Sun, J. Y. An anode-free potassium-metal battery enabled by a directly grown graphene-modulated aluminum current collector. *Adv. Mater.* **2022**, *34*, 2202902.
[47] Li, J. F.; Hu, Y. Y.; Xie, H. B.; Peng, J.; Fan, L.; Zhou, J.; Lu, B. A. Weak cation–solvent interactions in ether-based electrolytes stabilizing potassium-ion batteries. *Angew. Chem., Int. Ed.* **2022**, *61*, e202208291.
[48] Li, S. W.; Zhu, H. L.; Liu, Y.; Han, Z. L.; Peng, L. F.; Li, S. P.; Yu, C.; Cheng, S. J.; Xie, J. Codoped porous carbon nanofibres as a potassium metal host for nonaqueous K-ion batteries. *Nat. Commun.* **2022**, *13*, 4911.
[49] Yi, Y. Y.; Li, J. Q.; Gao, Z. X.; Liu, W. F.; Zhao, Y.; Wang, M. L.; Zhao, W.; Han, Y.; Sun, J. Y.; Zhang, J. Highly potassiophilic graphdiyne skeletons decorated with Cu quantum dots enable dendrite-free potassium-metal anodes. *Adv. Mater.* **2022**, *34*, 2202685.
[50] Sui, Y. M.; Liu, C. F.; Masse, R. C.; Neale, Z. G.; Atif, M.; AlSalhi, M.; Cao, G. Z. Dual-ion batteries: The emerging alternative rechargeable batteries. *Energy Storage Mater.* **2020**, *25*, 1–32.
[51] Küpers, V.; Dohmann, J. F.; Bieker, P.; Winter, M.; Placke, T.; Kolek, M. Opportunities and limitations of ionic liquid- and organic carbonate solvent-based electrolytes for Mg-ion-based dual-ion batteries. *ChemSusChem* **2021**, *14*, 4480–4498.
[52] Zhang, X.; Zhu, H. Z.; He, Q.; Xiong, T.; Wang, X. P.; Xiao, Z. T.; Wang, H.; Zhao, Y.; Xu, L.; Mai, L. Q. K^+ induced phase transformation of layered titanium disulfide boosts ultrafast potassium-ion storage. *Adv. Funct. Mater.* **2022**, *32*, 2205330.